Force production and flow structure of the leading edge vortex on flapping wings at high and low Reynolds numbers

James M. Birch*, William B. Dickson[†] and Michael H. Dickinson[†,‡]

Department of Integrative Biology, University of California, Berkeley, CA 94720, USA

*Present address: M Division, Physics and Advanced Technology, Lawrence Livermore National Laboratory, 7000 East Ave, Livermore, CA 94550-9234, USA

[†]Present address: California Institute of Technology, Mail Code 138-78, Pasadena, CA 91125, USA

[‡]Author for correspondence (e-mail: flyman@caltech.edu)

Summary

The elevated aerodynamic performance of insects has been attributed in part to the generation and maintenance of a stable region of vorticity known as the leading edge vortex (LEV). One explanation for the stability of the LEV is that spiraling axial flow within the vortex core drains energy into the tip vortex, forming a leading-edge spiral vortex analogous to the flow structure generated by delta wing aircraft. However, whereas spiral flow is a conspicuous feature of flapping wings at Reynolds numbers (*Re*) of 5000, similar experiments at *Re*=100 failed to identify a comparable structure. We used a dynamically scaled robot to investigate both the forces and the flows created by a wing undergoing identical motion at *Re* of ~120 and ~1400. In both cases, motion at constant angular velocity and fixed angle of attack generated a stable LEV with no evidence of shedding. At *Re*=1400, flow visualization indicated an intense narrow region of spanwise flow within the core of the LEV, a feature conspicuously absent at *Re*=120. The results suggest that the transport of vorticity from the leading edge to the wake that permits prolonged vortex attachment takes different forms at different *Re*.

Key words: insect flight, Reynolds number, aerodynamics, flow visualization.

Introduction

One of the challenges in developing a comprehensive theory of biological flight is to understand how aerodynamic mechanisms change with body size. Recent work has focused on flows generated by flapping wings in a variety of different-sized animals, including fruit flies (Birch and Dickinson, 2001, 2003), hawkmoths (Ellington et al., 1996; VandenBerg and Ellington, 1997b; Willmott et al., 1997), butterflies (Brodsky, 1991; Ellington et al., 1996; VandenBerg and Ellington, 1997b; Willmott et al., 1997) and birds (Pennycuick et al., 2000; Spedding et al., 1984; Tucker, 1995). The body size of a flying animal determines, for the large part, the Reynolds number (*Re*) at which its wings operate. Thus, the diversity of insect sizes virtually guarantees that they experience *Re* regimes ranging from 10 to 10 000. In order to understand the aerodynamic constraints on insects of different size, it is important to determine how wing performance changes with *Re*.

Research has identified the phenomenon of dynamic stall as an essential aerodynamic mechanism responsible for the elevated performance of flapping wings. Because of its importance, the influence of body size on aerodynamic performance will be determined in large part by the effects of *Re* on the forces generated by dynamic stall. A prominent leading edge vortex (LEV), the hallmark of dynamic stall, has been observed on the leading edge of model *Manduca* wings at *Re*=5000 and model *Drosophila* wings at *Re*=150. In *Drosophila*, this enlarged area of vorticity is prominent at angles of attack above ~12°, at which flow separates from the leading edge (Dickinson and Götz, 1993). The importance of the LEV was noted by Maxworthy in the context of Weis-Fogh's 'clap-and-fling' mechanism (Maxworthy, 1979, 1981). The formation of an LEV was examined on both tethered and model dragonfly wings by Luttges and colleagues (Somps and Luttges, 1985; Saharon and Luttges, 1987; Reavis and Luttges, 1988). In a seminal study, Ellington and colleagues (Ellington et al., 1996) visualized an LEV on the wing of a live hawkmoth in tethered flight (*Re*~4000). More recently, LEVs have been observed on butterfly wings in free flight (Srygley and Thomas, 2002). The topological structure of the LEV observed on butterfly wings during free flight differed somewhat from that observed on the robotic models. However, these experiments on real and model insects differed with respect to wing morphology, wing kinematics, *Re* and the presence or absence of a free stream flow. For these reasons, an explanation for the observed differences in flow structure remains obscure.

Two-dimensional studies, in which edge baffles inhibit

spanwise flow, show that the growth of the LEV begins at the start of translation and continues until the vortex becomes unstable, detaches from the leading edge and is shed into the wake. Subsequently, a counter-rotating vortex forms at the trailing edge, which grows and sheds, followed by the build-up of another LEV. The process continues, leaving a wake of counter-rotating vortex pairs known as a von Kármán street (Schlichting, 1979). In three-dimensional flapping, however, the LEV is stable at both high (5000) and low (120) Re (Usherwood and Ellington, 2002b). Although viscous dissipation may play a role, this stability must arise in large part from the transport of vorticity into the wake. In model hawkmoth wings, axial flow through the vortex core forms a spiral vortex, which has been proposed as the mechanism of transport that drains energy from the LEV (VandenBerg and Ellington, 1997a,b; Willmott et al., 1997). However, experiments at Re=120 failed to find evidence for either strong axial flow within the LEV core or a spiral structure (Birch and Dickinson, 2001). In addition, attempts to limit flow with fences and edge baffles did not significantly alter flows, forces or shedding dynamics.

These differences suggest that the transport of vorticity that maintains prolonged attachment may take different forms at different Re. However, prior experiments at low and high Re were performed using different methods and different wing shapes. To measure the influence of Reynolds number on flow structure and force production more accurately, we performed two sets of experiments using a dynamically scaled robotic insect using identical kinematics and wing geometry. To change Re from 120 to 1400, we changed only the viscosity of the fluid in which the robot flapped. Our results indicate that the presence of axial flow in the vortex core on model *Manduca* wings and its absence on model *Drosophila* wings is an effect of Re and not an artefact of differences in experimental methodology or due to differences in wing morphology.

Materials and methods

The dynamically scaled robot used in this study has been described before (Dickinson et al., 1999; Sane and Dickinson, 2001) and its construction will be briefly summarized here. The robot consisted of six servo-motors and two coaxial arms immersed in a tank of mineral oil, although only one arm and wing were used in this study. The acrylic wing was cut in the planform of a *Drosophila* wing with a total length of 0.26 m when attached to the coaxial arm. At the base of the wing, a sensor measured parallel and perpendicular forces from which we calculated total force or separate lift and drag force components. Force data were collected at 100 Hz using a Measurement Computing PCI-DAS1000 Multifunction Analog Digital I/O board (Measurement Computing, Middleboro, MA, USA) and filtered off-line using a zero phase delay low-pass digital Butterworth filter with a cut-off frequency of 10 Hz, roughly 60 times the wing stroke frequency. The wing and arm apparatus were placed in a 1 m×1.5 m×3 m Plexiglas tank filled with 1.8 m³ of mineral oil (Chevron Superla® white oil; Chevron Texaco Corp., San

Ramon, CA, USA). We changed Re by working with oil of two different viscosities. For low Re, we used oil with a density of $0.88×10^3$ kg m⁻³ and a kinematic viscosity of 120 centistokes (cSt). For high Re, we used oil with a density of $0.83×10^3$ kg m⁻³ and a kinematic viscosity of 11 cSt.

We calculated the translational force coefficients using the equations of Ellington (1984) derived from a blade element analysis:

$$C_L = \frac{2F_L}{\rho(\dot{\phi}R)^2 S \int_0^1 \hat{r}^2 \hat{c}(\hat{r})d\hat{r}} \qquad (1)$$

and

$$C_D = \frac{2F_D}{\rho(\dot{\phi}R)^2 S \int_0^1 \hat{r}^2 \hat{c}(\hat{r})d\hat{r}} \qquad (2)$$

where C_L and C_D are the lift and drag coefficients, respectively, F_L and F_D are the measured lift and drag forces, respectively, ρ is density, $\dot{\phi}$ is angular velocity, R is the length of one wing, S is wing surface area, and $\int_0^1 \hat{r}^2 \hat{c}(\hat{r})d\hat{r}$ represents the nondimensional second moment of area, where $\hat{r}$ is nondimensional wing length and $\hat{c}$ is nondimensional chord length. Forces were averaged during the center third of a 240° stroke in which the wingtip moves approximately 10 mean cord lengths at constant velocity and angle of attack. To measure aerodynamic polars, we varied the angle of attack from –10° to 110° in 10° increments.

Flow visualization

We used digital particle image velocimetry (DPIV) to quantify the flow structure around the wing while the wing translated at a 45° angle of attack. When the flow around the wing reached a steady state, a commercial software package controlling a dual Nd-YAG laser system (Insight v. 3.4; TSI Inc., St Paul, MN, USA) pulsed two identically positioned light sheets, approximately 2.5 mm thick, separated by 2 ms. A camera positioned perpendicular to these light sheets captured these two images. The fluid was seeded with visualization particles prior to image capture by either forcing air through a ceramic water filter stone or adding silver-coated glass beads (mean diameter, 13 μm; Conduct-o-fil®; Potters Industries, Inc., Valley Forge, PA, USA). When seeding with bubbles, we waited until larger bubbles rose to the surface. The remaining bubbles, although slightly positively buoyant, did not rise perceptively during capture of the paired DPIV images. Forces measured with bubbles or beads in the tank were identical to those measured in oil without additions, indicating that their introduction did not alter the basic properties of the medium. The wing was centered within two-dimensional DPIV images taken perpendicular to the long axis of the wing (i.e. from the side) and images taken parallel to the long axis of the wing (i.e. from the rear). The final data set consisted of 22 side views moving from $0.24R$ to $1.08R$ (where R is the length of one wing) in 1 cm increments. The laser and camera were then

moved to capture 15 rear views starting 3 cm in front of the leading edge and continuing until 3 cm behind the trailing edge, also in 1 cm increments. We merged these two views (side and rear) based on wing position within each slice creating a cube containing u_x, u_y and u_z velocities. A second data set of rear views was collected at high *Re*, with slices separated by only 0.5 cm to better ascertain flow patterns.

For each image pair captured, a cross-correlation of pixel intensity peaks with 50% overlap of 64 pixel×64 pixel interrogation areas yielded a 30×30 array of vectors. Vector validation removed vectors greater than 3 standard deviations of the mean vector length in their respective images. Deleted values were filled by interpolation of a mean value from a 3×3 nearest neighbor matrix. Sub-pixel displacement accuracy was approximately 0.1 pixel, resulting in 2.5% uncertainty for mean pixel displacements of 4 pixels. A custom program written in MATLAB was used to calculate vorticity from the velocity fields that had been smoothed using a least-squares finite difference scheme. All force and flow descriptions were captured during a stroke that started from rest; there was no wake influence from prior strokes.

To provide a qualitative representation of the flow field, we built a wing with a bubble rake consisting of a small plastic tube glued to the leading edge. Along the basal two-fifths of the wing, the tubing was punctured with small holes at approximately 1 cm intervals. This tube was attached to a pump that created small bubble streams that allowed flow visualization as the wing flapped. We used a Nikon D1X digital camera in continuous shooting mode (~9 frames s^{-1}) to capture images throughout the translation phase of flapping. We captured pictures of the wing at each *Re* when its orientation was approximately parallel to the camera.

Force estimates

Two methodologies were employed to estimate the aerodynamic forces from the velocity fields. The first and simplest method was based on the circulation theorem and only yields an estimate of lift. In this method, the sectional lift (L') at each spanwise position (z) was calculated using:

$$L'(z) = -\rho U_0(z)\Gamma_z(z) , \qquad (3)$$

where $U_0(z)=\phi z$ is the free steam velocity of the wing section and $\Gamma_z(z)$ is the circulation. The total lift experienced by the wing was then estimated by integrating the sectional forces along the span of the wing. The second method used to estimate the forces from the velocity field was a two-dimensional steady version of a method developed by Noca et al. (1997) and yields estimates of both lift and drag. In this method, the sectional force on the wing was calculated using:

$$\mathbf{F}' = \rho \int_A \mathbf{u} \times \boldsymbol{\omega}\, dA - \rho \oint_S \mathbf{n} \cdot \mathbf{u}(\mathbf{x} \times \boldsymbol{\omega})\, dS +$$
$$\oint_S \mathbf{n} \cdot \left[\mathbf{x} \cdot (\nabla \cdot \mathbf{T})\mathbf{I} - \mathbf{x}(\nabla \cdot \mathbf{T}) + \mathbf{T} \right] dS , \qquad (4)$$

where *A* is an area enclosing the wing section, *S* is the boundary of this area, **u** is velocity, **ω** is vorticity, **n** is the outward unit normal vector, **x** is the position vector, **T** is the stress tensor, and **I** is the unit tensor. Note, when employing this method in a 2-D manner, only the *x* and *y* components of the velocity field and the spanwise components of the vorticity field are utilized. The *x* and *y* components of the sectional force are the sectional drag, $D'(z)$, and sectional lift, $L'(z)$, estimates, respectively. As with the previous method (equation 3), the total lift and drag experienced by the wing can then be estimated by integrating the sectional lift and sectional drag along the span of the wing.

Results

Lift and drag coefficients during translation are consistent with prior measurements on three-dimensional wings (Dickinson et al., 1999). A wing starting from rest shows an initial force transient followed by constant force production (Fig. 1A). This stable force generation indicates prolonged attachment of the LEV for the full duration of the stroke. Mean coefficient values during one-third of translation (broken vertical lines in Fig. 1A) are plotted in the aerodynamic polars in Fig. 1B. Except at very low and very high angles of attack, the lift coefficients were higher at *Re*=1400. The drag coefficients at *Re*=1400 were less than the drag coefficients at *Re*=120 until an angle of attack of ~30°, presumably due to the contribution of viscous skin friction at low angles of attack. At high angles of attack, however, coefficients at *Re*=1400 were greater as total drag becomes dominated by pressure. The net force coefficients were higher at *Re*=1400 than *Re*=120 for all angles of attack greater than 30° (Fig. 1C). In addition, the net force vector approaches the angle of 90° to the wing surface slightly faster at higher *Re* (Fig. 1D), indicating a higher relative contribution of viscous drag at *Re*=120.

In side view, during translation the flow structure around the wing shows two areas of opposite vorticity (Fig. 2A). Above the leading edge and spreading rearward over the upper side of the wing is a large area of clockwise (CW) vorticity indicative of the leading edge vortex (LEV). Along the undersurface of the wing there exists a region of vorticity of the opposite sense (CCW) that we call the under-wing vorticity layer. Qualitative inspection of the vorticity plots shows a region of comparatively greater vorticity near the core of the LEV at *Re*=1400, a result consistent with the force measurements.

Integrating vorticity values over the entire panel provides an approximation of the local circulation around the wing (Fig. 2B). Measured along the wing from the base to the tip, local circulation shows a general increase at both *Re* until approximately 0.6*R*, where it decreases due to separation of the LEV and formation of the tip vortex. Circulation is greater at *Re*=1400 over most of the wing.

To illustrate the relationship between the LEV and the tip vortex, a rectangular control volume of infinitesimal width enclosing a wing section is chosen such that the vorticity flux across the top, bottom and front surfaces is zero, leaving only flux across the sides and rear of the volume. This can be done

by ensuring that the top, bottom and front faces are sufficiently far from the wing. The continuity law applied to vorticity requires that the sum of the fluxes across the sides and rear surfaces must be zero. Since the control volume has infinitesimal width, it can be shown that the rate of change in spanwise circulation with respect to span ($d\Gamma_z/dz$) is equal and opposite to the rate of change in chordwise circulation with respect to span ($-d\Gamma_x/dz$) along the back face of the control volume. Using the DPIV data, we can illustrate this relationship by comparing the spanwise circulation at each wing section to the chordwise circulation in the wake between the wing base at that section of the wing.

This comparison reveals a remarkable consistency between measures of spanwise (Γ_z) and chordwise (Γ_x) circulation

(Fig. 3A). For each increase in spanwise circulation along the span of the wing, there is a corresponding decrease in the chordwise circulation within the wake, as required by continuity. Except for a constant offset, the similarity between spanwise circulation along the wing and chordwise circulation within the wake indicates that these two flows might be accurately represented by a continuous array of vortex filaments that bend back into the wake.

In order to establish the relationship between the structure of the flows and the aerodynamic performance of wings, two methodologies were employed to estimate the aerodynamic forces from the velocity fields. The first method was based on the circulation theorem and yielded only lift estimates. The second method, a two-dimensional steady version of a method
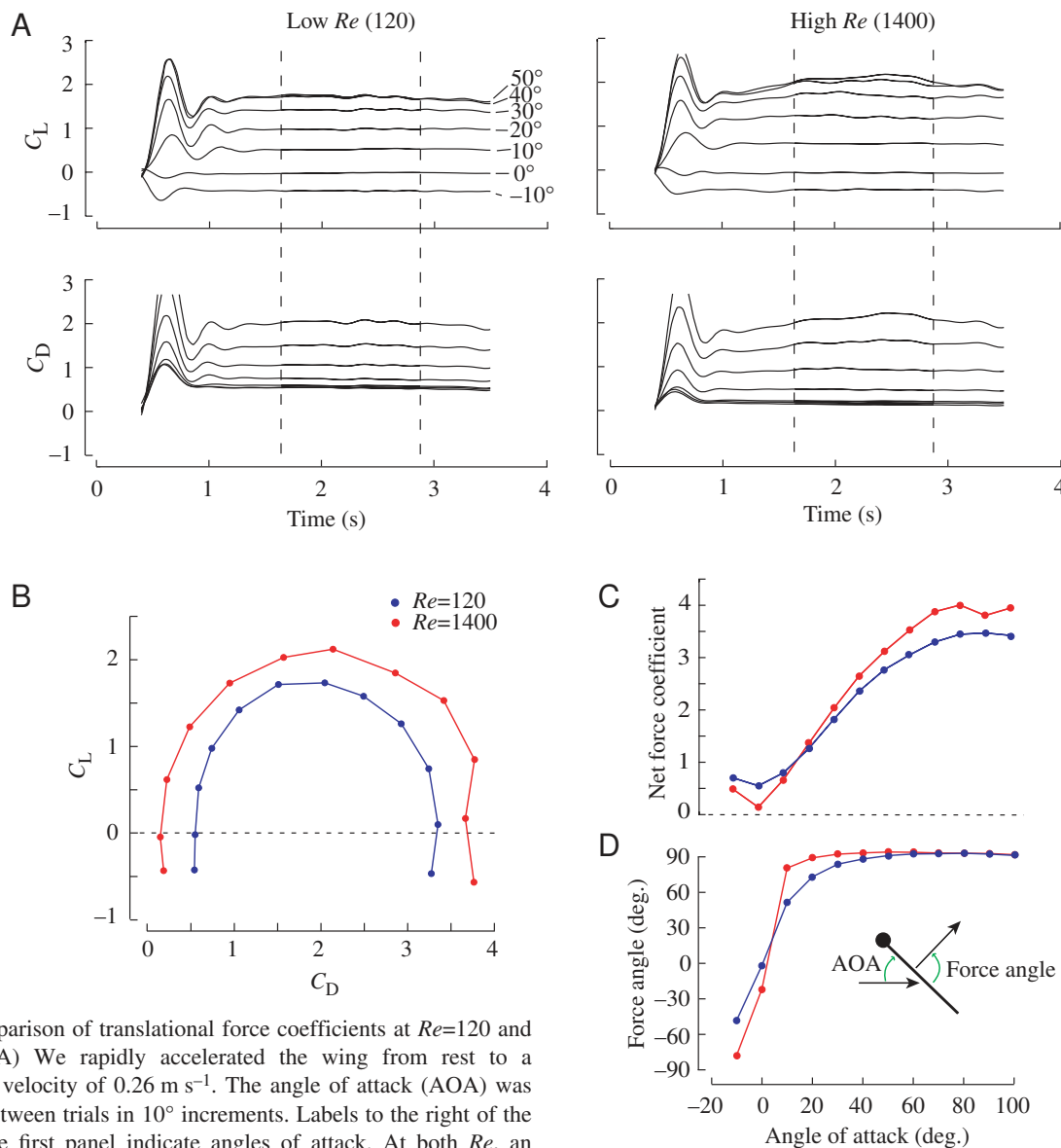

Fig. 1. Comparison of translational force coefficients at $Re=120$ and $Re=1400$. (A) We rapidly accelerated the wing from rest to a constant tip velocity of 0.26 m s^{-1}. The angle of attack (AOA) was increased between trials in 10° increments. Labels to the right of the forces in the first panel indicate angles of attack. At both Re, an initial transient peak was followed by stable force generation. (B) Coefficients of lift (C_L) and drag (C_D) averaged between the broken lines in A. The polars form two concentric arcs with values measured at high Re around the outermost arc. (C) Net force coefficients increase with angle of attack, with greater increases at high Re. (D) The angle of the net force vector quickly reaches 90°, indicating pressure forces dominate at both low and high Re.

developed by Noca et al. (1997), yielded both lift and drag estimates. For *Re*=120 and *Re*=1400, the estimates for lift from the circulation method were 0.3 N and 0.38 N, respectively. Comparing these estimates with the measured values of lift (0.44 N for *Re*=120 and 0.5 N for *Re*=1400) demonstrates that these simple estimates based on the circulation can account for approximately 70% of the lift produced by the wing. The lift estimated using the two-dimensional steady version of Noca's method was 0.37 N for *Re*=120 and 0.47 N for *Re*=1400, which is within 15% of the measured values. Whereas the lift estimates based on Noca's formula are closer to the measured values than those of the circulation method, both methods predict approximately the same difference in lift between the two *Re*. The reason for this can be found by considering the first term

of equation 4, (referred to as the Kutta–Zhukovski term in Noca, 1997): $\rho \int_A \mathbf{u} \times \boldsymbol{\omega} dA$. Decomposing the velocity field into free stream [$\mathbf{U_0}=(U_0,0,0)^T$] and perturbation ($\mathbf{u'}$) components so that $\mathbf{u}=\mathbf{U_0}+\mathbf{u'}$, the sectional lift component (*y*-component) of the Kutta–Zhukovski term, can then be written as:

$$\rho \int_A \mathbf{u} \times \boldsymbol{\omega} dA = -\rho \mathbf{U_0}(z)\Gamma_z(z) - \rho \int_A \mathbf{u'}\omega_z dA . \qquad (5)$$
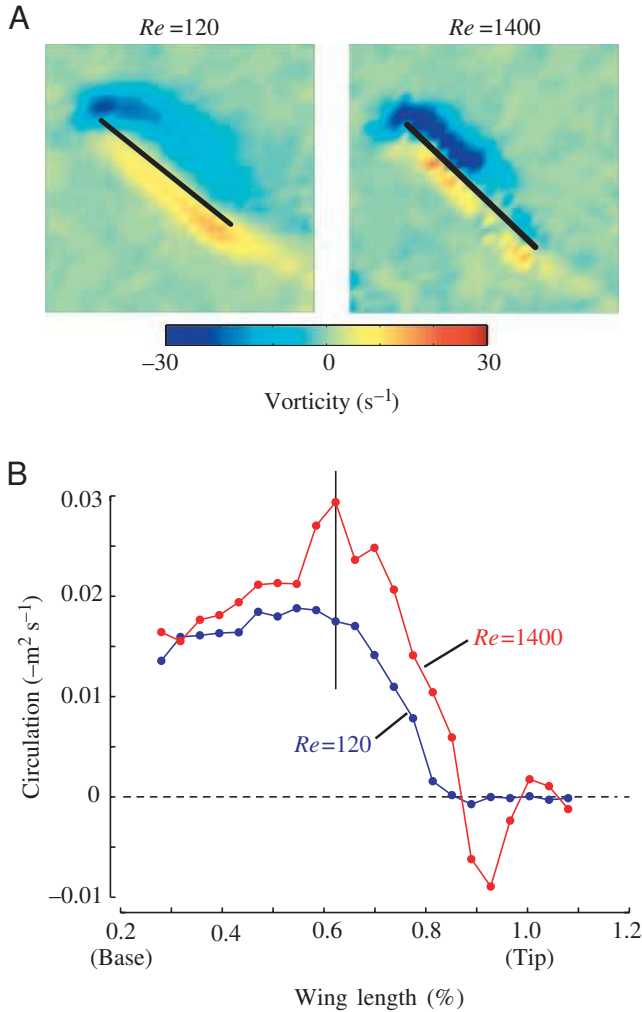
A

Fig. 2. Vorticity measurements at both *Re*. (A) Side views of wing at 0.65*R* (*R* is the length of one wing) at mid-downstroke. Wing is moving to the left at an angle of attack of 45°. Note the stronger and larger leading edge vortex at the higher *Re*. (B) Circulation around the wing as a function of wing length. The vertical line at 0.65*R* represents the position of the pseudocolor plots in A. The area of greatest vorticity shifts slightly towards the wingtip at high *Re*, occurring at 0.65*R* versus 0.49*R* at low *Re*.
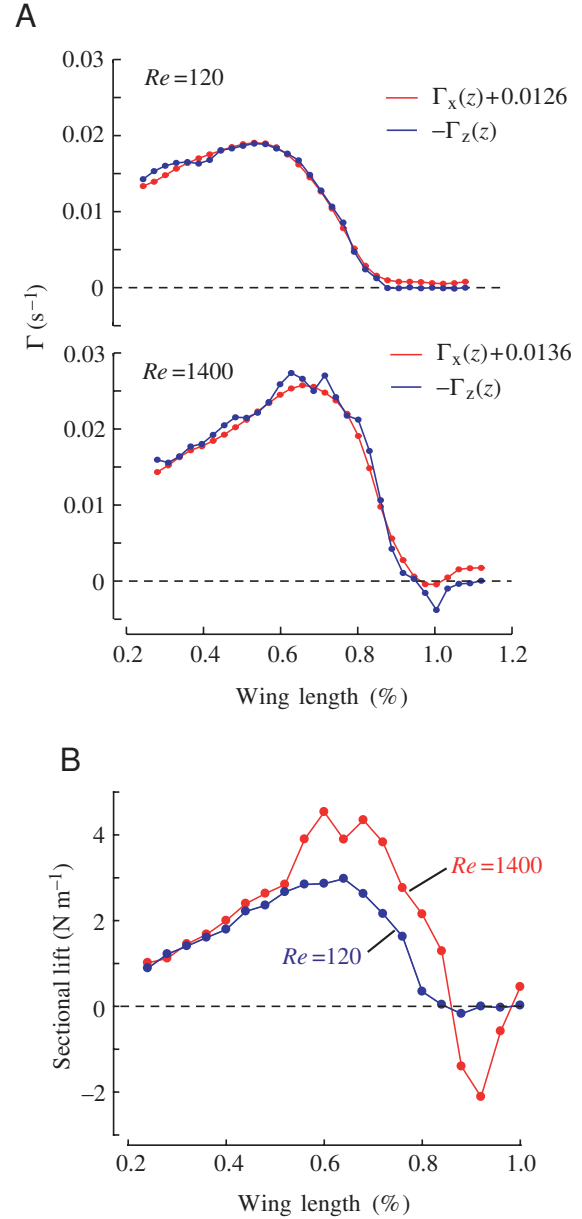
Fig. 3. Calculated circulation and subsequent force. (A) Although measurements were made during separate digital particle image velocimetry (DPIV) experiments, spanwise (Γ_z) and chordwise (Γ_x) circulation show similar strength profiles along the wing. (B) Using values for spanwise vorticity (ω_z) in the Kutta–Zhukovski equation, sectional lift values at both *Re* are maximum near 0.65*R*, with high *Re* generating more lift along the outer third of the wing.
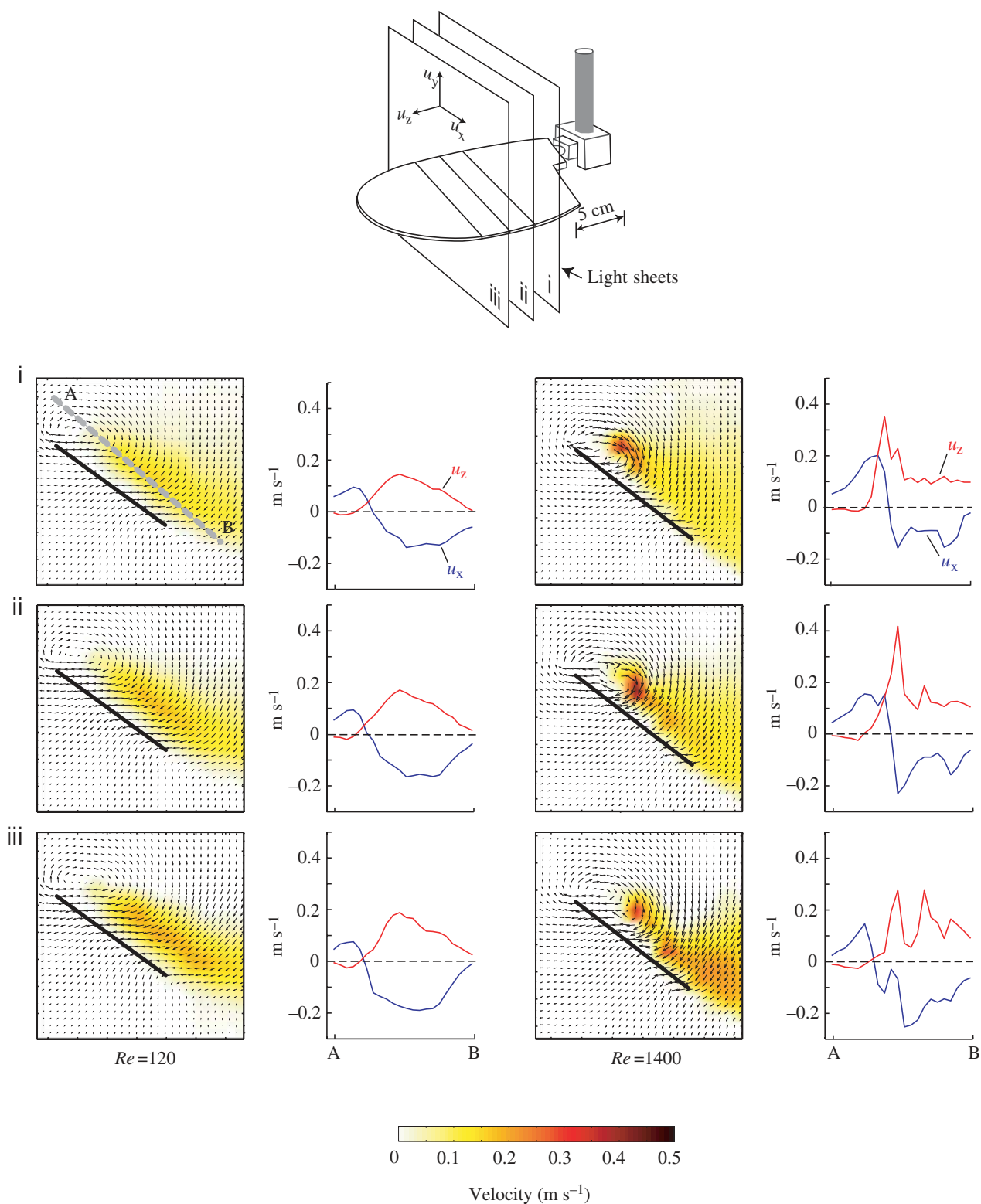
Fig. 4. The magnitude and distribution of axial flow is dependent on *Re*. The top schematic shows the position of the three side view panels (0.45*R*, 0.55*R* and 0.65*R*) at each *Re*. Flows are captured from a wing at mid-downstroke starting from rest. Columns 1 and 3 show the sectional velocity field as arrows (u_y and u_x) superimposed over a pseudo-color plot of axial velocity (u_z). Next to each column are plotted the u_x and u_z values along the gray broken transect from A to B shown in i. The left two columns show flow at low *Re*. Note how the maximum axial flow (u_z) at low *Re* occurs farther behind the vortex center than at high *Re*. Also, at high *Re*, flow near the leading edge is much more complicated, with a stronger axial flow component.
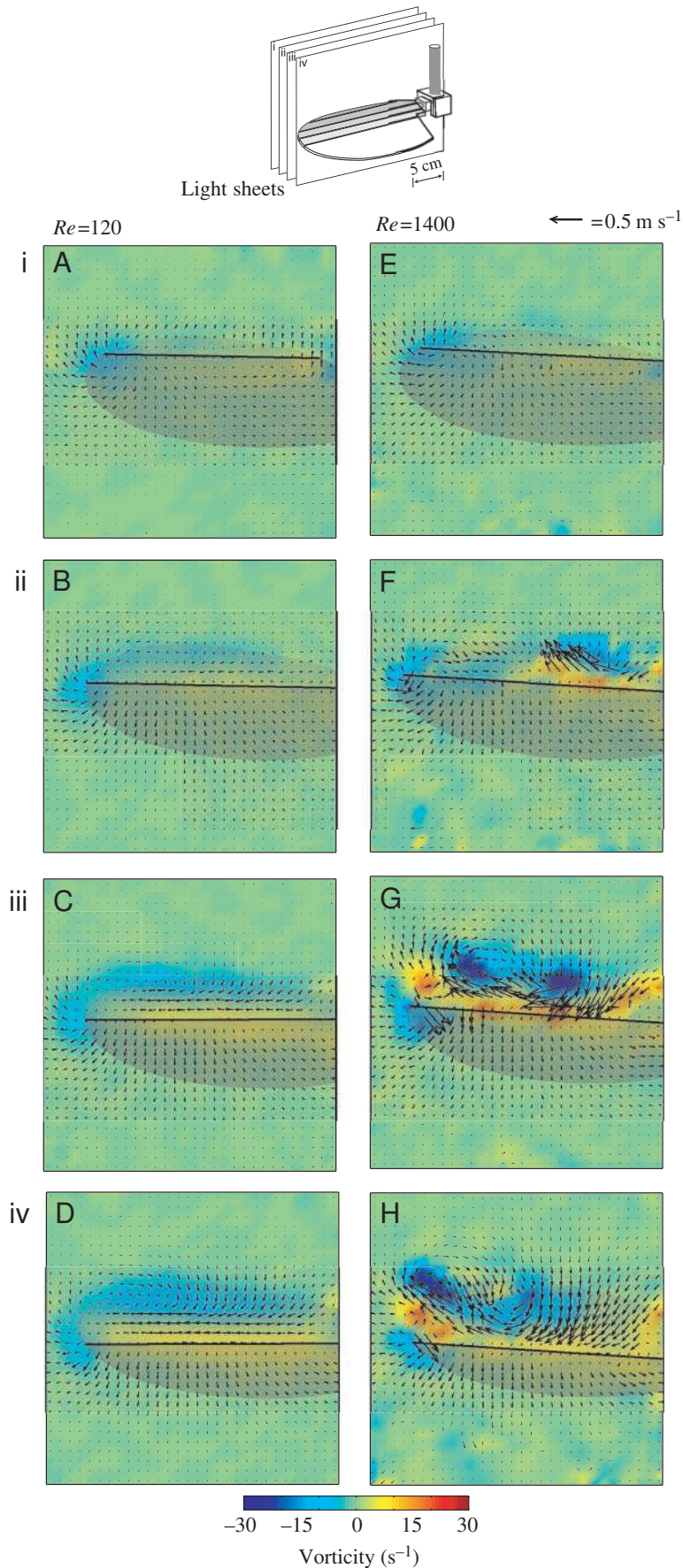
From this we can see that the sectional lift estimate based on the circulation is actually contained within the Kutta–Zhukovski term of Noca's formula. Thus, the contributions of the remaining terms to the difference in lift, everything except $-\rho U_0(z)\Gamma_z(z)$, must be small. This suggests that a large percentage of the lift experienced by the wing (~70%) at both *Re* (120 and 1400) is due to the spanwise circulation about the wing and that this difference in spanwise circulation at different *Re* can account for the differences in lift. The sectional lift predicted by the circulation method is shown in Fig. 3B.

The drag estimate from Noca's method yielded 0.18 N for *Re*=120, which was approximately 40% of the measured value, and 0.33 N for *Re*=1400, which was approximately 73% of the measured value. The reason for this inaccuracy in the drag estimates is unknown. The violation of two-dimensional flow, which we assumed in our calculation, is a likely candidate.

Flow visualizations display characteristic and consistent differences between *Re*. When fluid motion around the wing is viewed from the side, the LEV is evident at both *Re*=1400 and *Re*=120 (Fig. 4), although the flow pattern is more complicated at the higher *Re*. In Fig. 4, flow in three dimensions is shown by superimposing a pseudocolor plot to represent fluid velocity orthogonal to the field of the page (u_z). Next to each plot, we show the velocities in the *x* and *z* directions along a transect that passes through both the core of the LEV and the area of maximum axial flow. At *Re*=120, this tipward axial flow occurs over a broad region of the wing behind the LEV. There is no evidence of a peak in axial flow near the region of the vortex core, which is marked by the chordwise position at which u_x changes sign. By contrast, at *Re*=1400 an additional region of higher velocity axial flow within the core of the LEV is clearly visible, superimposed over a broad flow that is similar in structure to that present at *Re*=120. Furthermore, at *Re*=1400 the maximum axial flow within the core approaches velocities of 0.47 m s^{-1} at a spanwise position of 0.55*R*. This, value is significantly greater than the tip velocity

Fig. 5. Vorticity and velocity when viewed from behind. Color represents vorticity, arrows represent velocity (arrow scale upper right). Panels i–iv show successive slices starting just behind the leading edge (i) and moving toward the trailing edge in 1 cm increments (see inset at top). The solid horizontal line indicates the laser sheet intersection with the wing; vectors above this line are above and behind the wing, vectors below represent fluid movement as seen through the wing (i.e. below and in front of the wing). Columns (A–D and E–H) represent two experimental protocols with identical wing size, flapping frequency and kinematic pattern; only oil viscosity and *Re* are different.

of 0.31 m s^{-1}. As the view moves more towards the tip, the LEV becomes less cohesive and at least two regions of intense axial flow are apparent over the upper surface of the wing (Fig. 4iii).

Fig. 5 shows four successive views from the rear, beginning slightly behind the leading edge, each moving rearward by 1 cm. Fluid motion at Re=120 (left column) appears smooth and similar to views previously published (Birch and Dickinson, 2001). After fluid moves up over the leading edge (Fig. 5A), the fluid becomes entrained in the clockwise-rotating tip vortex. This entrainment manifests itself as a more pronounced base-to-tip movement of fluid in slices closer to the trailing edge (Fig. 5C,D). In each slice, fluid movement appears smooth and cohesive, particularly the base-to-tip movement of fluid above the wing and the rotation of the incipient tip vortex. At Re=1400 (Fig. 5E–H), the flow structure seen in two-dimensional slices within the area of the LEV shows a pattern hinting at the structure of a spiral vortex.

In Fig. 5F, the laser sheet intersects a region of high speed flow directed upward and distally. Moving rearward by 1 cm (Fig. 5G), the sheet continues to intersect a complicated base-to-tip movement but is now directed downward and distally. By Fig. 5H, the light sheet has moved behind the LEV and sections through an intense tip vortex.

In an attempt to more cleanly dissect the fluid structure within this region behind the leading edge, we performed another set of DPIV experiments where we positioned the camera to capture a closer view of the flow and separated slices by 0.5 cm (Fig. 6). The base-to-tip progression of a region of upward and distal directed flow in Fig. 6A–C suggests a spiral flow. Sections through the forming tip vortex (Fig. 6C–H) show a clear tip-to-base flow.

Photographs of wings equipped with a bubble rake provide further evidence for the existence of a spiral vortex at Re=1400. Fig. 7 shows photographs at mid-downstroke for both Re=120 (A,B) and Re=1400 (C,D) after the wing tip has traveled approximately three chord lengths. Beneath the full-wing photographs are three close-ups of the LEV at approximately 0.3 s intervals, showing the development (or lack thereof) of the spiral flow. At Re=120, while the bubbles trace a straight flow within the LEV core, there exists a slight twist in the bubble lines, imperceptible to DPIV analysis. At Re=1400, this slight twist has developed into a distinct spiral.

Discussion

With the use of a dynamically scaled robot and DPIV, we have quantified both the forces and fluid motion around an insect wing flapping at Re=120 and Re=1400. Our results show that stable forces and flows develop in both cases. This stability reaches different equilibrium points, as measured by net force and circulation, and is generated by qualitatively different flows. At both Re=120 and Re=1400, we observed no evidence of von
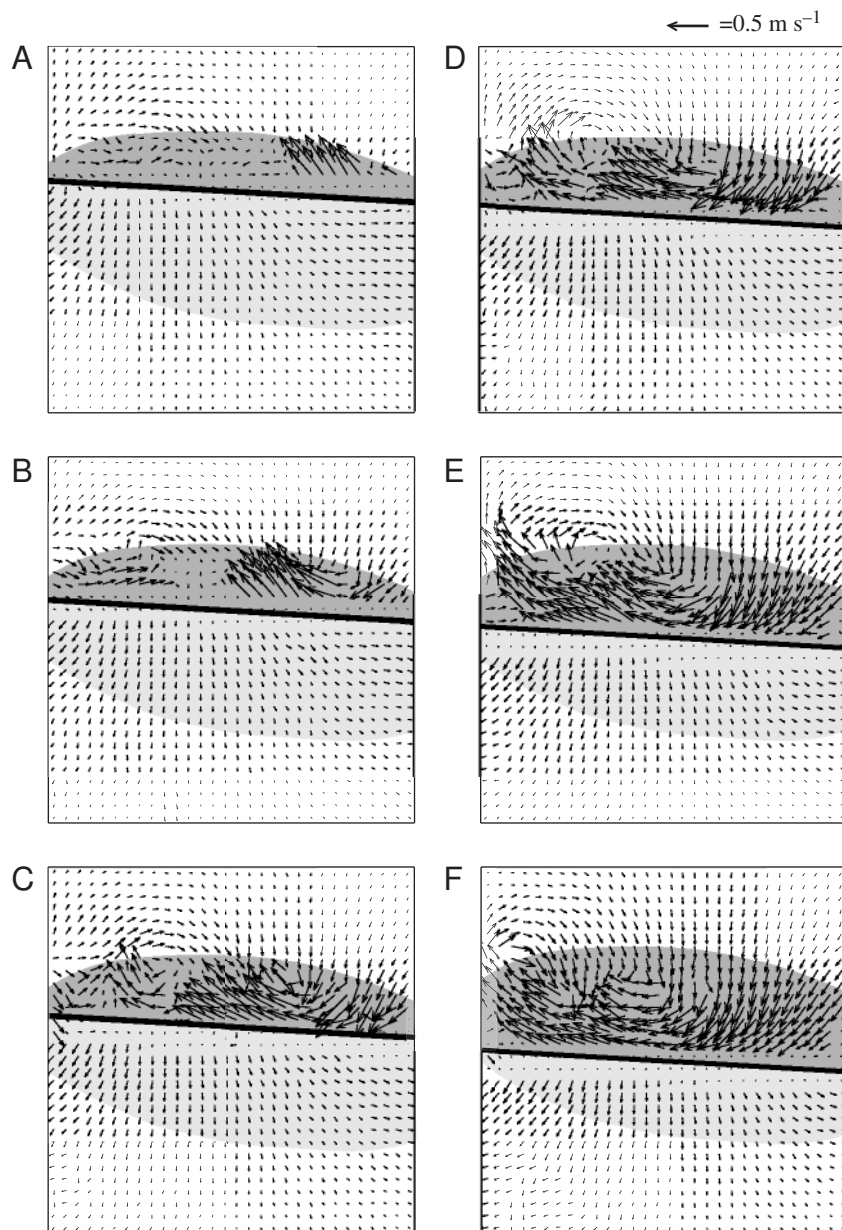

Fig. 6. Velocity vectors from the rear at Re~1400. These slices were captured in an identical fashion to those in Fig. 5 except that they were spaced every 0.5 cm with the camera closer to the wing. The wing tip is to the left, the leading edge (top) is into the page, the trailing edge (bottom) is out of the page, and the wing is sweeping away from the viewer and is caught during mid-downstroke. Note the localized high velocity movement of fluid in A and B, possibly representing the front edge of the spiral vortex. By E, the laser sheet is capturing the rear of the spiraling leading edge vortex.
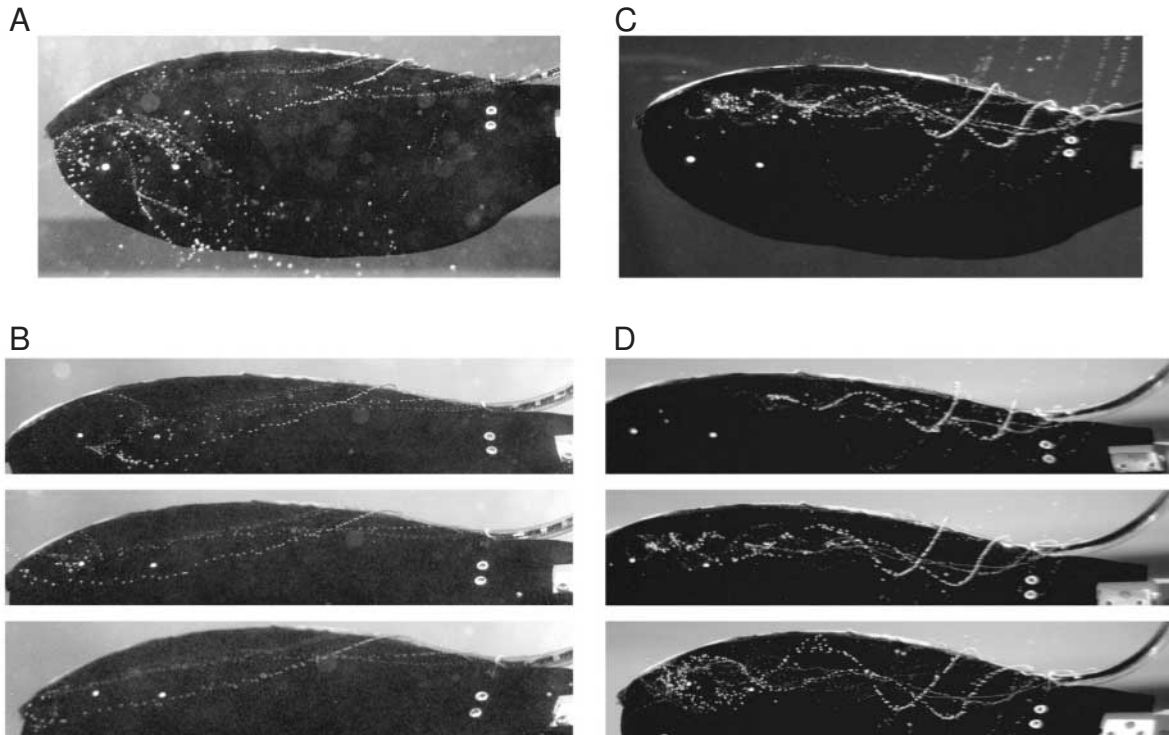
Fig. 7. Photographs near mid-downstroke using bubble rake. Left column (A,B) at *Re*=120. Right column (C,D) at *Re*=1400. Full wing views (A,C) taken at approximately mid-downstroke when wing is parallel to camera. Close-ups of the leading edge (B,D) show the growth of flow within the core of the leading edge vortex. Note the lack of a tight helix at low *Re* (B).

Kármán shedding, even though the amplitude of our strokes (270°) was beyond the morphological limit of any flapping animal (~180°). This stability (Dickinson et al., 1999; Usherwood and Ellington, 2002a) requires that the generation of vorticity at the leading edge (forming the LEV) must be balanced by a transport of vorticity into the wake. Results from this experiment indicate that this equilibrium is maintained over a range of *Re* from 120 to 1400. Evidence for this equilibrium was presented in earlier experiments in which a wall baffle and wing fences were used to impede spanwise flow at the wing tip (Birch and Dickinson, 2001). None of these conditions initiated shedding. However, the presence of the wall increased the size of the LEV, and resultant forces were higher [cf. fig. 1b and fig. 2c in Birch and Dickinson, 2001; note that scales on the vorticity plots are mislabeled and should range from –28 s⁻¹ to 28 s⁻¹; rear view (fig. 1d) from –20 s⁻¹ to 20 s⁻¹]. The role of induced flow (as mentioned in Birch and Dickinson, 2001) might be to decrease the rate at which vorticity is generated at the leading edge, but a transport mechanism is still required to maintain a stable equilibrium. Thus, neither inhibiting spanwise flow at *Re*=120 nor changing *Re* between 120 and 1400 affects the formation and stability of the LEV. It is not currently known whether inhibiting spanwise flow at *Re*=1400 would affect the formation and stability of the LEV.

While the LEV remains stable at both *Re*=120 and *Re*=1400, several conclusions can be drawn from the observed differences in flow structure. First, vortex transport *via* axial flow within the core of the LEV is not necessary for the stable attachment at *Re*=120. Forces and flows remain in equilibrium even when peak axial flow occurs behind the LEV, over the rear two-thirds of the wing (Fig. 4, first column), but not within the vortex core (Fig. 4, second column). A broad region of axial flow over the rear two-thirds of the wing is also present at *Re*=1400. However, in addition, we observed strong axial flow within the core of the LEV with velocities as high as 150% of wing tip speed. This secondary flow structure is clearly homologous to the spiral vortex identified by Ellington et al. (1996) and may contribute to the transport of vorticity into the wake. Second, flapping wings at *Re*=120 generate less circulation and lower forces, a result expected from the greater influence of viscosity. Furthermore, it is the decreased importance of viscosity that may account for the development of a spiral vortex at *Re*=1400. Whether this spiral flow is responsible for the elevation in circulation or whether both are independently related to the higher *Re* is not known.

How flow changes from the relatively simple pattern at *Re*=120 to spiral flow at *Re*=1400 is unclear. The emergence of the spiral vortex might be incremental or it might appear rapidly upon reaching some critical *Re*. Regardless of how it forms, such secondary flow structures are not unusual, especially when vortices transition to turbulent flow (see, for example, Berger, 1996; Leibovich, 1984). Even in experiments simulating two-dimensional conditions, vortices develop three-dimensional structures due to the asymmetries in the base vortex field or instabilities between consecutive vortices

(Julien et al., 2003). Thus, it is not surprising that we observed the development of the spiral vortex at higher Re, considering the instabilities introduced *via* the velocity gradient and subsequent non-uniform pressure distribution along the wing, as well as the curved leading edge. Whether this structure is a precursor to turbulent breakdown of the LEV or an epiphenomenon of its generation unrelated to stability remains to be determined.

List of symbols

A	area enclosing the wing section
$\hat{c}$	nondimensional chord length
C_D	drag coefficient
C_L	lift coefficient
$D'(z)$	sectional drag at each spanwise position
F_D	drag force
F_L	lift force
$\mathbf{I}$	unit tensor
$L'(z)$	sectional lift at each spanwise position
$\mathbf{n}$	outward unit normal vector
R	length of one wing
$\hat{r}$	nondimensional wing length
Re	Reynolds number
S	wing surface area
$\mathbf{T}$	stress tensor
$\mathbf{u}$	fluid velocity
$\mathbf{U_0}(z)$	free stream velocity of the wing section
$\mathbf{x}$	position vector
$\dot{\phi}$	angular velocity
Γ_x	chordwise circulation within the wake
Γ_z	spanwise circulation of the wing section
ρ	density
$\boldsymbol{\omega}$	vorticity

References

Berger, S. A. (1996). Vortex. In *McGraw-Hill 1997 Yearbook of Science and Technology* (ed. S. Parker), pp. 485-487. New York: McGraw-Hill.

Birch, J. M. and Dickinson, M. H. (2001). Spanwise flow and the attachment of the leading-edge vortex on insect wings. *Nature* **412**, 729-733.

Birth, J. M. and Dickinson, M. H. (2003). The influence of wing–wake interactions on the production of aerodynamic forces in flapping flight. *J. Exp. Biol.* **206**, 2257-2272.

Brodsky, A. K. (1991). Vortex formation in the tethered flight of the peacock butterfly *Inachis io* (Lepidoptera, Nymphalidae) and some aspects of insect flight evolution. *J. Exp. Biol.* **161**, 77-95.

Dickinson, M. H. and Götz, K. G. (1993). Unsteady aerodynamic performance on model wings at low Reynolds numbers. *J. Exp. Biol.* **174**, 45-64.

Dickinson, M. H., Lehmann, F. O. and Sane, S. (1999). Wing rotation and the aerodynamic basis of insect flight. *Science* **284**, 1954-1960.

Ellington, C. P. (1984). The aerodynamics of hovering insect flight. I. The quasi-steady analysis. *Phil. Trans. R. Soc. Lond. B* **305**, 1-15.

Ellington, C. P., VandenBerg, C., Willmott, A. P. and Thomas, A. L. R. (1996). Leading-edge vortices in insect flight. *Nature* **384**, 626-630.

Julien, S., Lasheras, J. and Chomaz, J. M. (2003). Three-dimensional instability and vorticity patterns in the wake of a flat plate. *J. Fluid Mech.* **479**, 155-189.

Leibovich, S. (1984). Vortex stability and breakdown – survey and extension. *AIAA J.* **22**, 1192-1206.

Maxworthy, T. (1979). Experiments on the Weis-Fogh mechanism of lift generation by insects in hovering flight. 1. Dynamics of the fling. *J. Fluid Mech.* **93**, 47-69.

Maxworthy, T. (1981). The fluid-dynamics of insect flight. *Annu. Rev. Fluid Mech.* **13**, 329-350.

Noca, F. (1997). On the evaluation of time-dependent fluid-dynamic forces on bluff-bodies. *Ph.D. Thesis*. Pasadena, CA: California Institute of Technology.

Noca, F., Shiels, D. and Jeon, D. (1997). Measuring instantaneous fluid dynamic forces on bodies, using only velocity fields and their derivatives. *J. Fluids Struct.* **11**, 345-350.

Pennycuick, C. J., Hedenstrom, A. and Rosen, M. (2000). Horizontal flight of a swallow (*Hirundo rustica*) observed in a wind tunnel, with a new method for directly measuring mechanical power. *J. Exp. Biol.* **203**, 1755-1765.

Reavis, M. A. and Luttges, M. W. (1988). Aerodynamic forces produced by a dragonfly. AIAA paper no. 88-0330.

Saharon, D. and Luttges, M. W. (1987). Three-dimensional flow produced by a pitching-plunging model dragon fly wing. AIAA paper no. 87-0121.

Sane, S. P. and Dickinson, M. H. (2001). The control of flight force by a flapping wing: lift and drag production. *J. Exp. Biol.* **204**, 2607-2626.

Schlichting, H. (1979). *Boundary-Layer Theory*. New York: McGraw-Hill.

Somps, C. and Luttges, M. (1985). Dragonfly flight – novel uses of unsteady separated flows. *Science* **228**, 1326-1329.

Spedding, G. R., Rayner, J. M. V. and Pennycuick, C. J. (1984). Momentum and energy in the wake of a pigeon (*Columba livia*) in slow flight. *J. Exp. Biol.* **111**, 81-102.

Srygley, R. B. and Thomas, A. L. R. (2002). Unconventional lift-generating mechanisms in free-flying butterflies. *Nature* **420**, 660-664.

Tucker, V. A. (1995). Drag reduction by wing tip slots in a gliding harris hawk, *Parabuteo unicinctus*. *J. Exp. Biol.* **198**, 775-781.

Usherwood, J. R. and Ellington, C. P. (2002a). The aerodynamics of revolving wings. I. Model hawkmoth wings. *J. Exp. Biol.* **205**, 1547-1564.

Usherwood, J. R. and Ellington, C. P. (2002b). The aerodynamics of revolving wings. II. Propeller force coefficients from mayfly to quail. *J. Exp. Biol.* **205**, 1565-1576.

VandenBerg, C. and Ellington, C. P. (1997a). The three-dimensional leading-edge vortex of a 'hovering' model hawkmoth. *Phil. Trans. R. Soc. Lond. B* **352**, 329-340.

VandenBerg, C. and Ellington, C. P. (1997b). The vortex wake of a 'hovering' model hawkmoth. *Phil. Trans. R. Soc. Lond. B* **352**, 317-328.

Willmott, A. P., Ellington, C. P. and Thomas, A. L. R. (1997). Flow visualization and unsteady aerodynamics in the flight of the hawkmoth *Manduca sexta*. *Phil. Trans. R. Soc. Lond. B* **352**, 303-316.